and the catalyst tolerates useful substrate functional groups, including aromatic and heteroatom substituents. With the development of improved methods for safe and scalable aerobic oxidation reactions (*30*), dehydrogenation methods of this type could have an important impact on laboratory- and industrial-scale chemical synthesis.

References and Notes

1. J. H. P. Tyman, *Synthetic and Natural Phenols* (Elsevier, New York, 1996).
2. R. E. Maleczka Jr., F. Shi, D. Holmes, M. R. Smith 3rd, *J. Am. Chem. Soc.* **125**, 7792 (2003).
3. S. S. Stahl, *Angew. Chem. Int. Ed.* **43**, 3400 (2004).
4. K. M. Gligorich, M. S. Sigman, *Chem. Commun.* **2009**, 3854 (2009).
5. X. Chen, K. M. Engle, D.-H. Wang, J.-Q. Yu, *Angew. Chem. Int. Ed.* **48**, 5094 (2009).
6. M. M. Konnick, S. S. Stahl, *J. Am. Chem. Soc.* **130**, 5753 (2008).
7. M. C. Denney, N. A. Smythe, K. L. Cetto, R. A. Kemp, K. I. Goldberg, *J. Am. Chem. Soc.* **128**, 2508 (2006).
8. P. Bamfield, P. F. Gordon, *Chem. Soc. Rev.* **13**, 441 (1984).
9. E. C. Horning, M. G. Horning, *J. Am. Chem. Soc.* **69**, 1359 (1947).
10. P. P. Fu, R. G. Harvey, *Chem. Rev.* **78**, 317 (1978).
11. T. Moriuchi, K. Kikushima, T. Kajikawa, T. Hirao, *Tetrahedron Lett.* **50**, 7385 (2009).
12. C. S. Yi, D. W. Lee, *Organometallics* **28**, 947 (2009).
13. P. F. Schuda, W. A. Price, *J. Org. Chem.* **52**, 1972 (1987).
14. J. Muzart, J. P. Pete, *J. Mol. Catal.* **15**, 373 (1982).
15. T. T. Wenzel, *J. Chem. Soc. Chem. Commun.* **1989**, 932 (1989).
16. J. Muzart, *Eur. J. Org. Chem.* **2010**, 3779 (2010).
17. D. R. Buckle, in *Encyclopedia of Reagents for Organic Synthesis*, D. Crich, Ed. (Wiley, New York, 2010).
18. J. Choi, A. H. R. MacArthur, M. Brookhart, A. S. Goldman, *Chem. Rev.* **111**, 1761 (2011).
19. R. Ahuja *et al.*, *Nat. Chem.* **3**, 167 (2011).
20. X. W. Zhang, D. Y. Wang, T. J. Emge, A. S. Goldman, *Inorg. Chim. Acta* **369**, 253 (2011).
21. R. C. Larock, T. R. Hightower, *J. Org. Chem.* **58**, 5298 (1993).
22. R. A. T. M. van Benthem, H. Hiemstra, J. J. Michels, W. N. Speckamp, *J. Chem. Soc. Chem. Commun.* **1994**, 357 (1994).
23. A. N. Campbell, P. B. White, I. A. Guzei, S. S. Stahl, *J. Am. Chem. Soc.* **132**, 15116 (2010).
24. Y. Izawa, S. S. Stahl, *Adv. Synth. Catal.* **352**, 3223 (2010).
25. L. H. Heitman *et al.*, *J. Med. Chem.* **52**, 2036 (2009).
26. R. A. Sheldon, J. M. Sobczak, *J. Mol. Catal.* **68**, 1 (1991).
27. J. E. Bercaw, N. Hazari, J. A. Labinger, *J. Org. Chem.* **73**, 8654 (2008).
28. J. E. Bercaw, N. Hazari, J. A. Labinger, P. F. Oblad, *Angew. Chem. Int. Ed.* **47**, 9941 (2008).
29. G. E. Dobereiner, R. H. Crabtree, *Chem. Rev.* **110**, 681 (2010).
30. X. Ye, M. D. Johnson, T. Diao, M. H. Yates, S. S. Stahl, *Green Chem.* **12**, 1180 (2010).

Acknowledgments: We are grateful to the NIH (RC1-GM091161), Mitsubishi Chemical Corporation, and NSF (CHE-1041934 to D.P.) for financial support of this work.

Supporting Online Material

www.sciencemag.org/cgi/content/full/science.1204183/DC1
Materials and Methods
Figs. S1 to S20
Tables S1 and S2
Characterization Data of New Compounds
References (*31*–*43*)

11 February 2011; accepted 1 June 2011
Published online 9 June 2011;
10.1126/science.1204183

High Pre-Eruptive Water Contents Preserved in Lunar Melt Inclusions

Erik H. Hauri,[1]* Thomas Weinreich,[2] Alberto E. Saal,[2] Malcolm C. Rutherford,[2] James A. Van Orman[3]

The Moon has long been thought to be highly depleted in volatiles such as water, and indeed published direct measurements of water in lunar volcanic glasses have never exceeded 50 parts per million (ppm). Here, we report in situ measurements of water in lunar melt inclusions; these samples of primitive lunar magma, by virtue of being trapped within olivine crystals before volcanic eruption, did not experience posteruptive degassing. The lunar melt inclusions contain 615 to 1410 ppm water and high correlated amounts of fluorine (50 to 78 ppm), sulfur (612 to 877 ppm), and chlorine (1.5 to 3.0 ppm). These volatile contents are very similar to primitive terrestrial mid-ocean ridge basalts and indicate that some parts of the lunar interior contain as much water as Earth's upper mantle.

The Moon is thought to have formed in a giant impact collision between a Mars-sized object and an early-formed proto-Earth (*1*). Though all of the inner planets, including Earth, are depleted in water and other volatiles when compared with primitive meteorites, the more extreme depletion of volatiles in lunar volcanic rocks has long been taken as key evidence for a giant impact that resulted in high-temperature catastrophic degassing of the material that formed the Moon (*2*, *3*). However, recent work on rapidly quenched lunar volcanic glasses has detected the presence of water dissolved in lunar magmas at concentrations up to 46 parts per million (ppm) (*4*), and water contents of lunar apatite grains from mare basalts are consistent with similarly minor amounts of water in primitive lunar magmas (*5*–*7*). These results indicate that the Moon is not a perfectly anhydrous planetary body and suggest that some fraction of the Moon's observed depletion in highly volatile elements may be the result of magmatic degassing during the eruption of lunar magmas into the near-vacuum of the Moon's surface.

To bypass the process of volcanic degassing, we conducted a search for lunar melt inclusions in Apollo 17 sample 74220, a lunar soil containing ~99% high-Ti volcanic glass beads, the so-called orange glass with 9 to 12 weight % (wt %) TiO_2 (*8*). Melt inclusions are small samples of magma trapped within crystals that grow in the magma before eruption. By virtue of their enclosure within their host crystals, melt inclusions are protected from loss of volatiles by degassing during magma eruption. Melt inclusions have been used for decades to determine pre-eruptive volatile contents of terrestrial magmas from subduction zones (*9*, *10*), hotspots (*11*, *12*), and mid-ocean ridges (*13*, *14*), as well as volatile contents of martian magmas (*15*, *16*). Using standard petrographic methods, we identified nine inclusion-bearing olivine crystals (Fig. 1) and analyzed melt inclusions hosted within (*17*). The measured water contents of the melt inclusions range from 615 ppm to a maximum of 1410 ppm (Fig. 2); these water contents are up to 100 times as high as the water content of the matrix glass surrounding the olivine crystals (6 to 30 ppm H_2O) and the centers of individual volcanic glass beads from the same sample (*4*). The melt inclusions also contain high concentrations of fluorine (50 to 78 ppm), sulfur (612 to 877 ppm), and chlorine (1.5 to 3.0 ppm) that are 2 to 100 times as high as those of the matrix glasses and individual glass beads from this sample (Fig. 3). Volatile contents corrected for postentrapment crystallization are on average 21% lower than the measured concentrations (*17*) and represent the best estimate of the pre-eruptive concentrations of volatiles in the 74220 magma.

There are few descriptions in the literature of melt inclusions contained within olivine from lunar samples, but these existing observations provide important context for the volatile abundances we have observed. Roedder and Weiblen (*18*–*20*) noted the presence of silicate melt inclusions in the first samples returned from the Apollo 11, Apollo 12, and Luna 16 missions and reported that many primary melt inclusions contained a vapor bubble, requiring dissolved volatiles to have been present in the melt at the time it was trapped within the host crystal. Klein and Rutherford (*21*) and Weitz *et al.* (*22*) found sulfur contents of 600 to 800 ppm, similar to our

[1]Department of Terrestrial Magnetism, Carnegie Institution of Washington, Washington, DC 20015, USA. [2]Department of Geological Sciences, Brown University, Providence, RI 02912, USA. [3]Department of Geological Sciences, Case Western Reserve University, Cleveland, OH 44106, USA.

*To whom correspondence should be addressed. E-mail: ehauri@ciw.edu

measurements, and Cl contents of <50 ppm that were limited by electron microprobe detection limits. Reheated Apollo 12 melt inclusions, containing medium-Ti magmas (5 to 6 wt % TiO_2), show sulfur contents that are 20% higher than our data on average (*23*). In our data set, we observe a correlation of all the volatiles with each other (Fig. 3), pointing toward the degassed compositions of the matrix glass rinds and volcanic glass beads (*4*).

The most important aspect of our volatile data on lunar melt inclusions is their similarity to melt inclusions from primitive samples of terrestrial mid-ocean ridge basalts (MORBs), like those recovered from spreading centers located within transform faults (*24*); the melt inclusions from 74220 are markedly similar to melt inclusions from the Siqueiros Fracture Zone on the East Pacific Rise, some of the most primitive mid-ocean ridge magmas that have been measured (Fig. 3). These similarities suggest that the volatile signature of the lunar mantle source of the high-Ti melt inclusions is very similar to that of the upper mantle source of MORB.

It is important that we have made these measurements on inclusions from olivine crystals contained within primitive lunar volcanic glasses. These inclusions were quenched within minutes after their eruption (*4*), providing minimal opportunity for posteruptive hydrogen diffusion out of the inclusions and affording a direct H_2O measurement on primary lunar magma samples that have not experienced posteruptive degassing and associated loss of volatiles. The water concentrations that we measured are 20 to 100 times as high as previous direct measurements of the lunar glass beads from this same sample, which was estimated to have suffered 95 to 98% loss of H_2O via degassing (*4*), and they are higher than estimates derived from lunar apatite measurements, which require a 95 to 99% correction for fractional crystallization to estimate primary magma volatile contents (*5*, *6*). Our results are direct measurements on primary lunar magma compositions that require no such extrapolations.

Our melt inclusion data allow us to place some constraints on the volatile content of the lunar mantle source that generated the high-Ti picritic magmas. Using the most water-rich melt inclusion composition after correction for post-entrapment crystallization, and an estimation that the high-Ti magmas originated from 5 to 30% batch partial melting with partitioning similar to that of terrestrial mantle-derived melts (*17*), we estimate lunar mantle volatile concentrations of 79 to 409 ppm H_2O, 7 to 26 ppm F, 193 to 352 ppm S, and 0.14 to 0.83 ppm Cl. These estimates overlap most estimates for the volatile content of the terrestrial MORB mantle (*24*–*27*) and are much higher than previous estimates for the lunar mantle based on the volatile content of lunar apatite (*5*, *6*) and the variation of Cl isotopes in lunar rocks (*28*), including the sample 74220 that we have studied here. The melt inclusions indicate definitively that some reservoirs within the interiors of Earth and the Moon not only have similar water contents, but also similar contents of fluorine, sulfur, and chlorine associated with this water, a volatile abundance signature shared by both bodies.

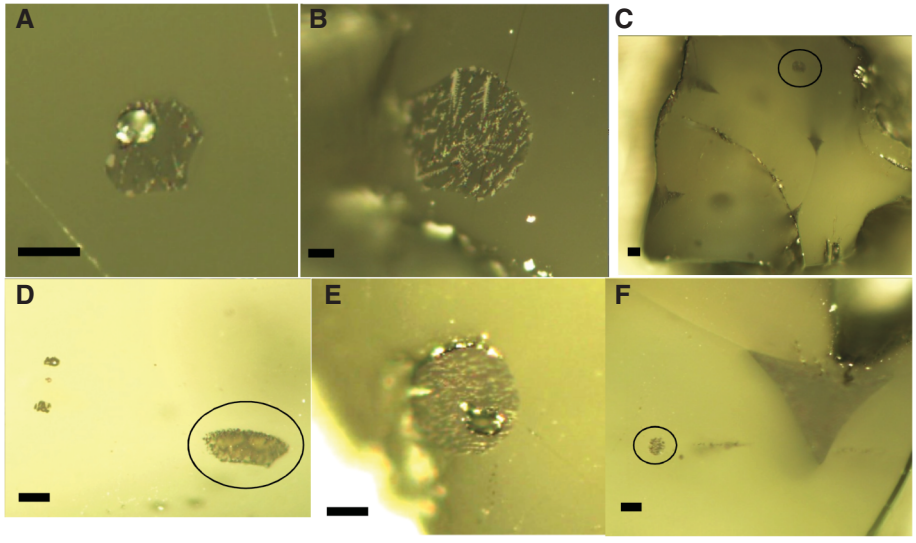

Fig. 1. (**A** to **F**) Optical photographs of olivines A1, A2, N3, N6, N8, and N9 from Apollo 17 sample 74220. Inclusions within circles indicate the inclusions that were imaged in Fig. 2. Scale bars are 10 μm in all photos.

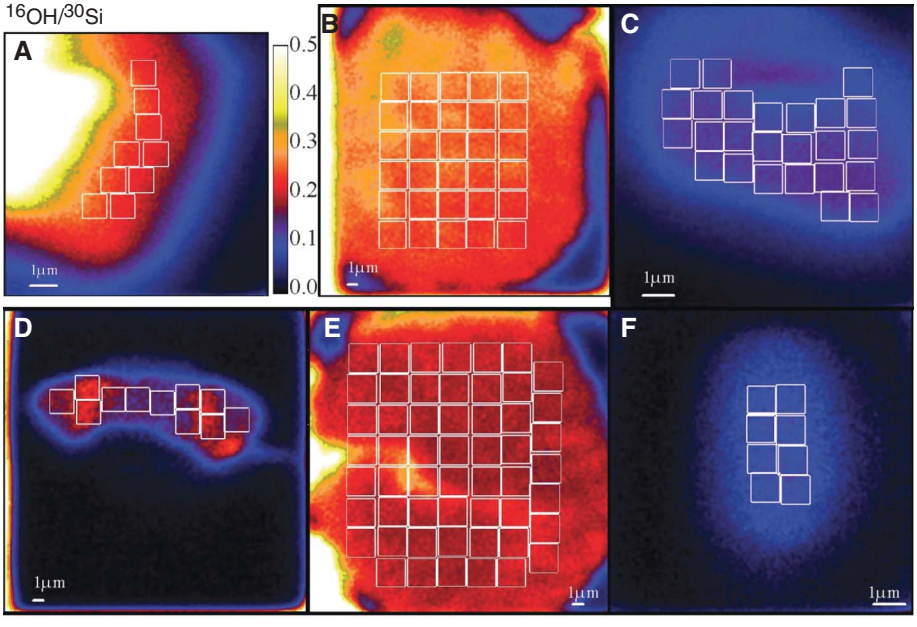

Fig. 2. (**A** to **F**) NanoSIMS scanning isotope images of olivines A1, A2, N3, N6, N8, and N9 from Apollo 17 sample 74220, showing the distribution of water within melt inclusions from the olivine grains shown in Fig. 1. The images show the distribution of the isotope ratio $^{16}OH/^{30}Si$ indicated by the color scale shown in (A), which ranges from dark regions corresponding to low $^{16}OH/^{30}Si$ ratios (e.g., olivine surrounding melt inclusions), to red regions within melt inclusions with $^{16}OH/^{30}Si$ ratios approaching 0.25 (corresponding to ~1400 ppm H_2O). The color scale is the same in all images, and all images show a scale bar of 1 μm. Rectangular areas are regions of interest within which each isotope ratio is calculated and converted to a concentration.

These results show that the Moon is the only planetary object in our solar system currently identified to have an internal reservoir with a volatile content similar to that of Earth's upper mantle, and that previous estimates of the lunar inventory for highly volatile elements are biased to low concentrations owing to the degassed nature of lunar samples thus far studied. The Moon has erupted a wide variety of magmas during its history, and it remains to be seen whether other

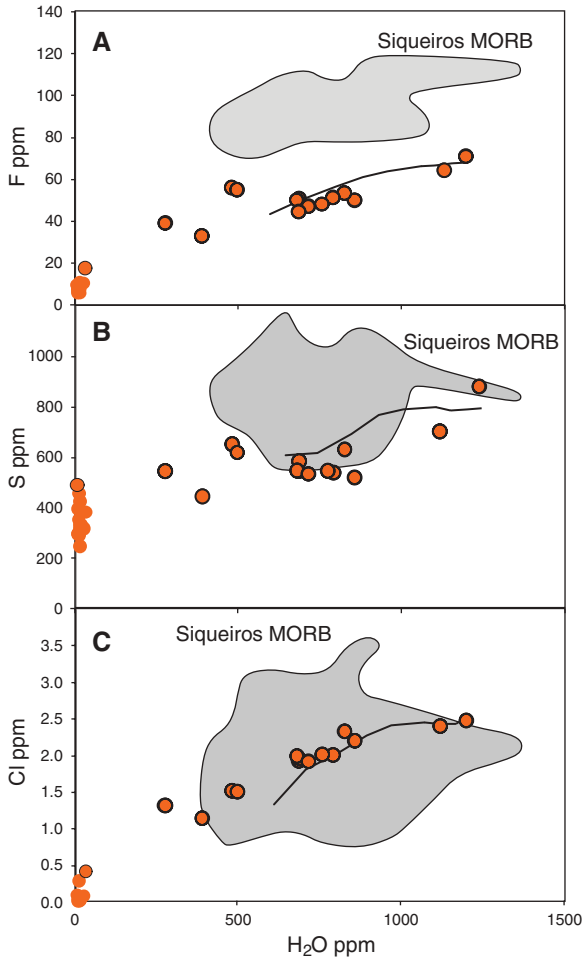

Fig. 3. (**A** to **C**) Volatile abundances for lunar melt inclusions (orange circle with black rims) and matrix glasses (orange circles) from Apollo 17 sample 74220. Melt inclusions show the highest concentrations (>600 ppm H_2O) whereas matrix glasses show the lowest concentrations due to degassing (≤30 ppm H_2O). The black curves show lunar magma degassing trends, scaled from the volatile-volatile correlations observed in core-rim NanoSIMS data on a lunar glass bead reported by Saal *et al*. (*4*); the core-rim data were scaled by multiplying the originally reported data for each element, by the ratio of the highest melt inclusion composition to that of the core composition reported in table 2 of (*4*). The gray field surrounds data for melt inclusions from the Siqueiros Fracture Zone on the East Pacific Rise, as an example of depleted MORB (*24*).

lunar mantle sources are as volatile rich as the source of Apollo 17 high-Ti magmas. Nevertheless, the hydrated nature of at least part of the Moon's interior is a result that is not consistent with the notion that the Moon lost its entire volatile inventory to the vacuum of space during degassing after a high-energy giant impact, which would be expected to leave a highly desiccated lunar interior.

If the bulk of the lunar interior has a volatile content similar to our estimate for the high-Ti mantle source, then our results present difficulties for late-accretion models that require volatile delivery to Earth and the Moon after their formation, because these two bodies have very different accretion cross sections that would predict different internal volatile contents. An Earth-Moon similarity in volatiles could indicate that chemical exchange of even the most volatile elements between the molten Earth and the proto-lunar disc might have been pervasive and extensive, resulting in homogenization at the very high temperatures expected after a giant impact; this could have been aided by the presence of a high-temperature convective atmospheric envelope surrounding Earth and the proto-lunar disc as the Moon solidified (*29*). Alternatively, it is conceivable that a portion of the lunar interior escaped the widespread melting expected in the aftermath of a giant impact and simply inherited the inventory of water and other volatiles that is characteristic of Earth's upper mantle. Any model for the formation of Earth-Moon system must meet the constraints imposed by the presence of H_2O in the lunar interior, with an abundance similar to that of Earth's upper mantle and with a complement of fluorine, sulfur, and chlorine also present at terrestrial levels. To the extent that lunar formation models predict very different volatile contents of Earth and the Moon, our results on the volatile content of lunar melt inclusions suggest that we lack understanding on some critical aspects of the physics of planetary moon formation by collisional impact.

Our findings also have implications for the origin of water ice in shadowed lunar craters, which has been attributed to cometary and meteoritic impacts (*30*). It is conceivable that some of this water could have originated from magmatic degassing during emplacement and eruption of lunar magmas (*31*). These results also underscore the importance of pyroclastic volcanic samples in unraveling the history and composition of the Moon's interior; indeed, such deposits have been identified and mapped on the surfaces of all the terrestrial planets and many satellites.

References and Notes

1. R. M. Canup, *Annu. Rev. Astron. Astrophys.* **42**, 441 (2004).
2. S. R. Taylor, in *Origin of the Moon*, W. K. Hartmann, R. J. Phillips, G. J. Taylor, Eds. (Lunar Planetary Institute, Houston, TX, 1986), pp. 125–143.
3. F. Albarède, *Nature* **461**, 1227 (2009).
4. A. E. Saal *et al*., *Nature* **454**, 192 (2008).
5. F. M. McCubbin *et al*., *Proc. Natl. Acad. Sci. U.S.A.* **107**, 11223 (2010).
6. J. W. Boyce *et al*., *Nature* **466**, 466 (2010).
7. J. P. Greenwood *et al*., *Nat. Geosci.* **4**, 79 (2011).
8. J. W. Delano, *J. Geophys. Res.* **91**, D201 (1986).
9. K. A. Kelley *et al*., *J. Geophys. Res.* **111**, B09208 (2006).
10. A. M. Shaw, E. H. Hauri, T. P. Fischer, D. R. Hilton, K. A. Kelley, *Earth Planet. Sci. Lett.* **275**, 138 (2008).
11. E. H. Hauri, *Chem. Geol.* **183**, 115 (2002).
12. J. C. Lassiter, E. H. Hauri, I. K. Nikogosian, H. G. Barsczus, *Earth Planet. Sci. Lett.* **202**, 525 (2002).
13. N. Shimizu, *Phys. Earth Planet. Inter.* **107**, 183 (1998).
14. A. M. Shaw, M. D. Behn, S. E. Humphris, R. A. Sohn, P. M. Gregg, *Earth Planet. Sci. Lett.* **289**, 311 (2010).
15. H. Y. McSween Jr., R. P. Harvey, *Science* **259**, 1890 (1993).
16. L. L. Watson, I. D. Hutcheon, S. Epstein, E. M. Stolper, *Science* **265**, 86 (1994).
17. Detailed information on melt inclusion identification and analytical methods used in this study, as well as all data, are contained in supporting online materials available at *Science* Online.
18. E. Roedder, P. W. Weiblen, *Proc. Lunar Sci. Conf.* **1**, 801 (1970).
19. E. Roedder, P. W. Weiblen, *Proc. Lunar Sci. Conf.* **2**, 507 (1971).
20. E. Roedder, P. W. Weiblen, *Earth Planet. Sci. Lett.* **13**, 272 (1972).
21. N. Klein, M. J. Rutherford, *Lunar Planet. Sci.* **29**, 1448 (1998).
22. C. M. Weitz, M. J. Rutherford, J. W. Head III, D. S. McKay, *Meteorit. Planet. Sci.* **34**, 527 (1999).
23. D. J. Bombardieri, M. D. Norman, V. S. Kamenetsky, L. V. Danyushevsky, *Meteorit. Planet. Sci.* **40**, 679 (2005).
24. A. E. Saal, E. H. Hauri, C. H. Langmuir, M. R. Perfit, *Nature* **419**, 451 (2002).
25. A. Jambon, J. L. Zimmermann, *Earth Planet. Sci. Lett.* **101**, 323 (1990).
26. P. Michael, *Earth Planet. Sci. Lett.* **131**, 301 (1995).
27. J. E. Dixon, L. Leist, C. Langmuir, J. G. Schilling, *Nature* **420**, 385 (2002).
28. Z. D. Sharp, C. K. Shearer, K. D. McKeegan, J. D. Barnes, Y. Q. Wang, *Science* **329**, 1050 (2010).
29. K. Pahlevan, D. J. Stevenson, *Earth Planet. Sci. Lett.* **262**, 438 (2007).
30. W. C. Feldman *et al*., *J. Geophys. Res.* **106**, 23231 (2001).
31. A. P. S. Crotts, *Astrophys. J.* **687**, 692 (2008).

Acknowledgments: This work was supported by the Carnegie Institution of Washington, the NASA LASER and Cosmochemistry programs, the NASA Lunar Science Institute, and the NASA Astrobiology Institute. We thank J. Wang for NanoSIMS assistance, and L. Nittler and Z. Peeters for help with image processing software.

Supporting Online Material

www.sciencemag.org/cgi/content/full/science.1204626/DC1
Materials and Methods
Figs. S1 and S2
Tables S1 and S2
References (*32*–*37*)

21 February 2011; accepted 10 May 2011
Published online 26 May 2011;
10.1126/science.1204626

www.sciencemag.org/cgi/content/full/science.1204626/DC1

Supporting Online Material for

High Pre-Eruptive Water Contents Preserved in Lunar Melt Inclusions

Erik H. Hauri,* Thomas Weinreich, Alberto E. Saal,
Malcolm C. Rutherford, James A. Van Orman

*To whom correspondence should be addressed. E-mail: ehauri@ciw.edu

Published 26 May 2011 on *Science* Express
DOI: 10.1126/science.1204626

This PDF file includes:

Supporting Online Material

Materials & Methods

The samples were examined at high magnification, and optical photographs of each olivine and each melt inclusion were obtained (Fig. 1). The inclusions are primary and of ovoid shape, with the exception of one inclusion that is triangular and appears to have been trapped between several olivine sub-grains (Fig. 1D). The inclusions contain variable proportions of glass (~70%), quench-textured olivine (~30%), occasional crystals of an oxide phase that is probably ilmenite, and vapor bubbles in two inclusions. Of the fourteen inclusions, seven were large enough for analysis, six were too small for analysis, and one inclusion consisted mainly of metal and was not analyzed. Seven of the olivine crystals also contained a matrix glass rind that surrounded the exterior of the crystal, and these glasses were analyzed as well.

In order to eliminate the possibility of volatile element diffusion during the interaction of an electron beam with the samples, we performed all of the SIMS volatile analyses prior to analyzing the samples for major elements. Major element analyses were performed using a JEOL Superprobe at the Carnegie Institution of Washington's Geophysical Laboratory. We used a 30nA beam focused to 1-2 μm for olivine analyses, and defocussed to 10μm for glass analyses; standardization was checked by reproducing the major element compositions of 74220 glass beads reported previously (*4*). Melt inclusions and matrix glass rinds consisted of ~70% glass and ~30% quench crystals of olivine, and their bulk compositions were measured by averaging a number of analyses distributed around the full exposure of the inclusion. We also conducted traverses of olivine adjacent to melt inclusions, and found no evidence for Fe-rich rims that exceeded 1 μm in width; even these are subject to possible phase boundary excitation, which can occur over 2-3 μm length scales. Average 2σ reproducibility of melt inclusion and matrix glass major elements is Si (1.4%), Ti (9.6%), Al (9.6%), Fe (2%), Mn (6%), Mg (13%), Ca (18%), Na (14%), K (17%) and P (17%). Average 2σ reproducibility of olivine analyses is 3-6% for all elements reported.

Major element compositions are reported in Table S1. The melt inclusions are contained in olivine with forsterite contents that range from $Fo_{80.5}$ to $Fo_{82.2}$. Melt inclusion MgO contents range from 3.3% to 13.4% and overlap the range of compositions displayed by matrix glass rinds on the outside of the host olivines, and volcanic glass beads from this same sample (Fig. S1). The melt inclusions exhibit post-entrapment olivine crystallization that ranged from 5.4% to 36%, averaging 21%; matrix glass rinds exhibit a similar average amount of post-entrapment crystallization (19%). After correction for this crystallization, the MgO contents of the 74220 melt inclusions (11.8% to 15.3%) are at the high end of the range of MgO observed in 74220 glass beads (max. 15.4% MgO), demonstrating their primitive compositions.

Analyses for volatile abundances were performed using the Cameca NanoSIMS 50L scanning ion microprobe at the Carnegie Institution of Washington's Department of Terrestrial Magnetism. A primary ion beam of Cs was used as the probe, rastering over an area of 30x30μm or 10x10μm, and negatively charged ions of the isotopes ^{16}OH, ^{19}F, ^{30}Si, ^{32}S and ^{35}Cl were measured simultaneously on six electron multipliers using ion counting. For every analysis location, we first performed a pre-sputtering step on a 30x30μm area for 2 minutes with a 10nA primary beam, then switched to a primary beam of 1nA on a 30x30μm or 10x10μm area for data acquisition. We used basaltic glass ALV519-4-1 as a standard to determine relative sensitivity factors for H_2O, F, S and Cl, and we used synthetic forsterite to monitor the detection limits of these elements, as

described previously (*32,33*). Mass resolving power of the instrument was set to ~6000 in order to resolve ^{16}OH from ^{17}O as well as other isobaric interferences; average ^{30}Si count rates were on the order of 200,000 cps. For standardization and detection limit determinations, we obtained data in two different modes of operation: standard Dynamic SIMS, and Scanning Ion Imaging SIMS. For the measurements of lunar melt inclusions and matrix glasses, only Scanning Ion Imaging SIMS was used and it is this data that is reported in Table S2.

Dynamic SIMS

In this mode of operation, only ion counts are recorded as data with no associated imaging. We divided the rastered area into 64x64 pixels and utilized a 245µm dwell time on each pixel (equivalent to 1 second per frame); we collected 50 cycles of data at 1 second per cycle, and corrected the data for system deadtime (electronically set to 44 ns). To eliminate stray ions from the edge of the crater that contribute to high background counts, we enabled electronic beam blanking to record data only from the innermost pixels from within the central of 3.7x3.7µm of the 10x10µm sputter crater, or within the central 11x11µm of a 30x30µm crater.

Scanning Ion Imaging SIMS

In this mode of operation, the instrument was used in an identical fashion as with Dynamic SIMS, except that the sputter crater was divided into 256x256 pixels and beam blanking was not used. Data were recorded as scanning ion images obtained simultaneously on each mass (^{16}OH, ^{19}F, ^{30}Si, ^{32}S and ^{35}C); in this mode, acquisition of a single frame takes ~16 seconds, and 10 frames were acquired at each analysis location, resulting in a total acquisition time of ~3 minutes.

Data were extracted and processed from the ion images using the L'Image software package for PV Wave written by Larry Nittler (DTM-CIW). Data were first corrected for system deadtime, and the last nine images were summed (first image used as a presputter); images were ratioed to produce scanning isotope ratio images ($^{16}OH/^{30}Si$, $^{19}F/^{30}Si$, $^{32}S/^{30}Si$ and $^{35}Cl/^{30}Si$), and data were extracted from specific user-defined regions of interest (ROIs) located within the isotope ratio images. Each ROI consisted of a unique 25x25 or 75x75 pixel area of the image (equivalent to 0.8x0.8µm similar to the beam diameter for a 10x10µm image, or ~3 beam diameters for a 30x30µm image) and a number of ROIs were specified for each isotope ratio image so that they did not overlap, were contained within the inclusion without overlapping host olivine, and did not overlap areas of containing surface contamination of volatiles (vapor bubble in Fig. 2A, crater edges in Fig. 2B,D,E). The isotope ratio images for standards and synthetic forsterite are essentially homogeneous (to within a few percent) except at the crater edges; for isotope ratio images of melt inclusions, the NanoSIMS sample stage was adjusted so that the inclusion was centered in the sputter crater prior to presputtering and image acquisition. For images of standards and synthetic forsterite, 30 ROIs were located in the center of the image; for images of melt inclusions, the number of ROIs varied from 6 (for small inclusions) to 36 (for large melt inclusions, see Figure 2); ROIs were located in the most homogeneous areas of the isotope ratio images, and verified to avoid overlap with host olivines and/or vapor bubbles guided by photographs of each melt inclusion taken prior to the NanoSIMS measurements, scaled to the size of the imaged area on the sample.

Within each ROI, the total number of ^{30}Si ion counts averaged around 200,000; for synthetic forsterite, average counts per ROI were 314 for ^{16}OH, 35 for ^{19}F, 22 for ^{32}S,

and 5.7 for ^{35}Cl. For basaltic glass standard ALV519-4-1, average counts per ROI were 117,000 for ^{16}OH (1700 ppm H2O), 83,000 for ^{19}F (95 ppm F), 492,000 for ^{32}S (950 ppm S), and 22,000 for ^{35}Cl (42 ppm Cl). The size of the ROIs and the number of images acquired were chosen so that, in general, the ROI was similar to the primary beam diameter, and the theoretical precision of each isotope ratio in each ROI was on the order of a few percent. For ALV519-4-1 standard, the 2-sigma reproducibility of all the ROIs was 5% or better for all elements. For synthetic forsterite used to measure detection limits, the 2-sigma reproducibility of the ROIs was 20% for H_2O, 34% for fluorine, 43% for sulfur, and 98% for chlorine – these were directly related to the total number of counts per ROI.

Comparison of Scanning Ion Imaging SIMS with Dynamic SIMS

An important part of the methods development for this study involved verification that the same isotope ratios could be obtained from Dynamic SIMS and processing of data from images obtained by Scanning Ion Imaging SIMS, in effect providing a ground-truthing of both scanning ion imaging and data processing methods. This was demonstrated on the ALV519-4-1 basaltic glass standard (for calibration purposes) and the synthetic forsterite (for detection limit purposes). For this comparison, we made five different measurements of each, in which each measurement was subjected to presputtering (as described above), followed by a Dynamic SIMS measurement (lasting 1 minute), followed lastly by a Scanning Ion Image acquisition (lasting 3 minutes). The data show that the isotope ratios obtained from both methods agree to within 3% on average, over a dynamic range of almost 5 orders of magnitude (isotope ratio values from ~5e-4 to 1.3, see Figure S2). From these measurements, the data for ALV519-4-1 were used to calculate the relative sensitivity calibrations for H_2O, F, S and Cl (using count rates normalized to ^{30}Si) while the data from synthetic forsterite were used to measure the detection limits of the same elements (7ppm H_2O, 0.06 ppm F, 0.07 ppm S and 0.02 ppm Cl).

Data for Lunar Melt Inclusions

Using standard petrographic methods, we identified fourteen inclusions in nine olivine crystals; seven of the inclusions were large enough for accurate analysis, seven were too small, and one was an inclusion of metal. Only Scanning Ion Imaging SIMS was used to obtain data on the lunar melt inclusions so as to preserve the material for future measurements; nevertheless, one of the viable melt inclusions (74220-N9#1) was sufficiently thin that it sputtered away during an attempted repeat analysis. The isotope ratio data were extracted from a number of ROIs located within each inclusion, the data from individual ROIs was corrected for detection limits, and an average concentration and 2-standard error uncertainty for each image acquisition was obtained by averaging the ROI data for each analysis. The "repeat" analyses in Table S1 indicate separate repeat image acquisitions obtained on the same melt inclusion (for olivines N3, N6 and N8); two melt inclusions were located in olivine N9 and a single image acquisition was obtained for each.

Errors reported in Table S2 are the average 2-sigma standard errors for the melt inclusion and matrix glass volatile data; these errors include the propagated uncertainties (as 2 standard deviations) of the detection limits, and are a measure of the precision of each image acquisition. Repeat image acquisitions of the same melt inclusions agree at a level that is similar to the calculated precision. Accuracy of the data is on the order of 5-10% (2-sigma) as indicated by the calibration discussion in Hauri et al. (*34*).

The major element data indicate that some degree of post-entrapment crystallization of olivine has occurred on the inside walls of these melt inclusions; there are no discernable compositional rims at the inclusion-olivine boundaries that exceed 1 μm in width, and even these are subject to possible phase boundary excitiation which can occur over length scales of 2-3 μm. As anticipated, the measured melt inclusion compositions fall within the range of compositions displayed by 74220 glass beads; this is also true for the matrix glass at the edges of olivine crystals. The olivines range from $Fo_{80.5}$ to $Fo_{82.2}$. The Fe-Mg Kd values for inclusion-olivine pairs range from 0.060 to 0.245; these values are lower than expected and are consistent with post-entrapment crystallization (PEC).

The amount of PEC determined from the major element data has a correspondingly minor effect on the volatile contents of the melt inclusions. We calculated melt inclusion compositions corrected for PEC of olivine in the standard fashion, by adding back equilibrium olivine in 0.1% increments, recalculating the melt composition at each step, until the melt inclusions arrived at Fe-Mg equilibrium with their host olivine crystals, indicated by an olivine-melt Kd value of 0.250 to 0.280. It is important to note that, at the high TiO_2 contents of our melts, olivine-melt Kd values are inversely correlated with melt TiO_2 contents, as demonstrated previously in several experimental studies *(35-37)*, and this effect is included in our correction for post-entrapment crystallization. The corrected melt inclusion compositions overlap completely with the highest MgO glass beads from 74220, and indicate that the inclusions experienced PEC of olivine varying from 5.4% up to 33% (average 21%, Table S1); these amounts of PEC are essentially identical for melt inclusions and associated matrix glasses.

The corrected volatile contents in Table S2 have been reduced by the amount of post-entrapment crystallization determined for each inclusion or matrix glass; for inclusion N9 #2, we corrected the volatile contents by the same amount as inclusion N9 #1 in the same crystal (27%); for inclusion N3, we corrected the volatile contents by the average amount of inclusion PEC (21%). These corrections (5.4% to 33%) are minor compared with the 20-100X difference between the melt inclusions and glass beads from this sample.

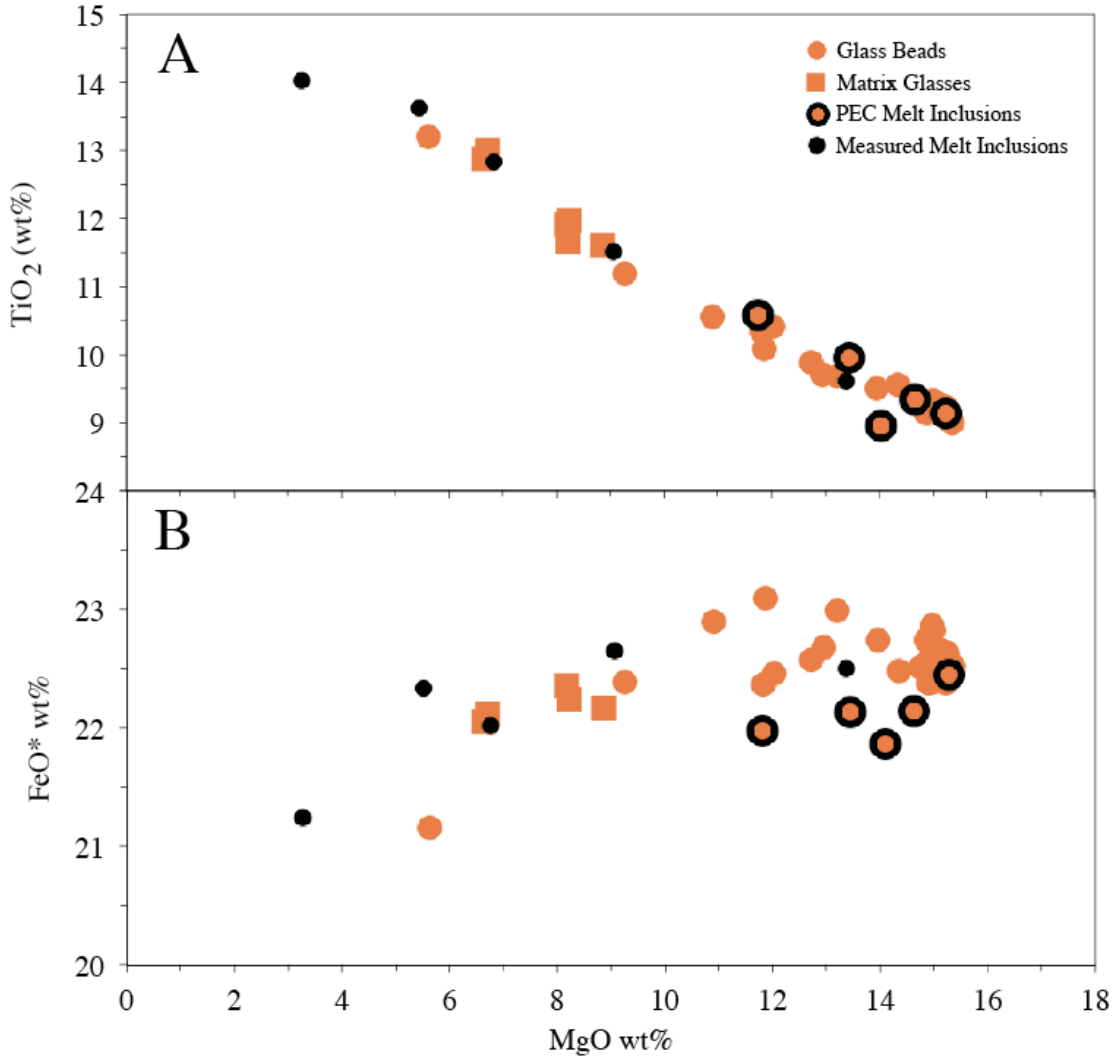

Figure S1. Major elements of melt inclusions from Apollo 17 sample 74220, showing compositions measured for melt inclusions and matrix glasses, and inclusions corrected for post-entrapment crystallization (PEC), compared with compositions for glass beads (*4*). The slightly lower FeO* contents for PEC-corrected melt inclusions may be the result of fractionation of small amounts of iron metal prior to inclusion entrapment, which we have not accounted for.

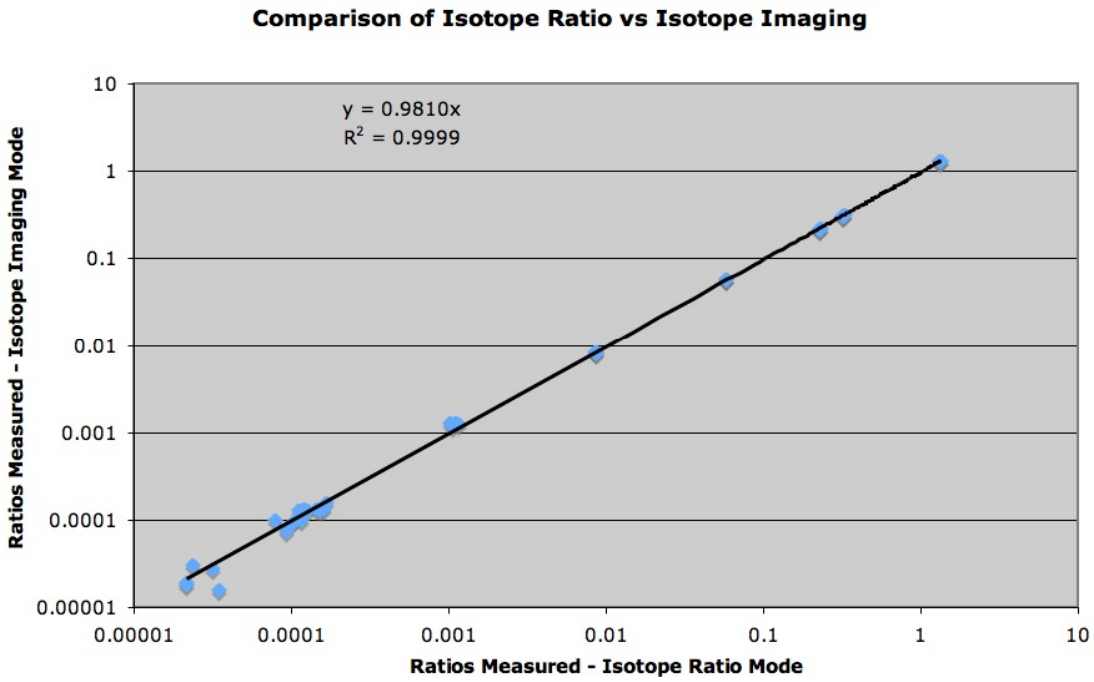

Figure S2. Comparison of isotope ratios measured by Dynamic SIMS (Isotope Ratio Mode) and Scanning Ion Imaging (Isotope Imaging Mode), using measurements obtained within the same sputter craters in synthetic forsterite and our basalt glass standard (ALV519-4-1).

Table S1. Major element compositions of melt inclusions, olivine crystals, and matrix glasses

Melt Inclusions	**SiO_2**	**TiO_2**	**Al_2O_3**	**FeO***	**MnO**	**MgO**	**CaO**	**Na_2O**	**K_2O**	**P_2O_5**	**Total**
A1 mi	38.83	9.63	6.24	22.51	0.25	13.37	7.75	0.33	0.06	0.03	98.993
A2 mi	39.63	11.51	7.01	22.66	0.28	9.06	10.17	0.40	0.07	0.02	100.83
N6 mi	39.58	12.90	8.35	22.02	0.28	6.78	11.07	0.42	0.08	0.03	101.50
N8 mi	40.37	14.03	10.34	21.25	0.30	3.28	15.14	0.54	0.07	0.03	105.36
N9 mi	39.84	13.65	8.68	22.33	0.30	5.51	12.23	0.42	0.08	0.03	103.07
Matrix Glasses											
A4 glass	39.48	11.61	7.04	22.17	0.31	8.86	9.79	0.30	0.05	0.02	99.65
N3 glass	39.00	11.92	7.16	22.36	0.28	8.18	10.20	0.36	0.07	0.03	99.56
N5 glass	39.29	11.67	7.15	22.25	0.29	8.21	10.10	0.36	0.07	0.03	99.41
N6 glass	39.63	13.00	7.68	22.12	0.29	6.71	11.08	0.44	0.08	0.03	101.08
N8 glass	40.02	12.87	7.57	22.05	0.29	6.64	11.09	0.38	0.06	0.03	101.01
N9 glass	39.01	11.97	7.22	22.50	0.27	8.23	10.38	0.36	0.07	0.03	100.03

Olivines	**SiO_2**	**TiO_2**	**Cr_2O_3**	**FeO***	**MnO**	**MgO**	**NiO**	**CaO**	**Total**	**Mg#**	**Kd (Fe-Mg)**
A1	39.28	0.10	0.34	17.67	0.21	42.85	0.02	0.24	100.71	0.81	0.245
A2	39.44	0.14	0.34	17.32	0.19	43.07	0.01	0.24	100.76	0.82	0.161
A4	39.67	0.11	0.35	17.80	0.22	43.02	0.02	0.24	101.43	0.81	0.165
N3	38.67	0.11	0.35	17.59	0.20	41.36	0.01	0.24	98.53	0.81	0.156
N5	38.43	0.11	0.34	17.42	0.19	42.78	0.02	0.24	99.53	0.81	0.150
N6	38.92	0.30	0.44	19.72	0.22	41.23	0.04	0.26	101.13	0.79	0.147
N7	38.90	0.12	0.34	18.02	0.20	42.65	0.01	0.24	100.48	0.81	
N8	39.60	0.13	0.33	17.21	0.19	44.18	0.01	0.24	101.91	0.82	0.060
N9	38.85	0.14	0.34	17.53	0.19	42.22	0.02	0.25	99.54	0.81	0.102

Corrected Melts	**SiO_2**	**TiO_2**	**Al_2O_3**	**FeO***	**MnO**	**MgO**	**CaO**	**Na_2O**	**K_2O**	**P_2O_5**	**%PEC[1]**
A1 mi	39.17	9.11	5.91	22.46	0.24	15.27	7.33	0.31	0.06	0.02	5.40
A2 mi	39.18	9.34	5.69	22.13	0.23	14.67	8.25	0.32	0.06	0.02	18.87
N6 mi	38.85	10.62	6.88	22.00	0.23	11.80	9.11	0.35	0.07	0.02	17.66
N8 mi	38.16	8.94	6.59	21.91	0.19	14.07	9.65	0.34	0.05	0.02	36.26
N9 mi	38.55	9.97	6.34	22.14	0.22	13.44	8.93	0.31	0.06	0.02	27.01
A4 glass	39.48	9.71	5.89	22.03	0.26	14.12	8.19	0.25	0.04	0.02	16.36
N3 glass	39.08	9.86	5.93	22.31	0.23	13.76	8.44	0.30	0.06	0.02	17.24
N5 glass	39.37	9.49	5.82	22.16	0.23	14.35	8.21	0.29	0.05	0.02	18.70
N6 glass	39.05	10.75	6.34	22.18	0.24	11.81	9.16	0.37	0.07	0.02	17.36
N8 glass	39.38	9.73	5.72	21.86	0.22	14.37	8.38	0.29	0.05	0.02	24.45
N9 glass	38.94	9.75	5.88	22.30	0.22	14.09	8.45	0.29	0.06	0.02	18.56

[1] Percentage of post-entrapment crystallization of host olivine

Table S2. Volatile contents of lunar melt inclusions from Apollo 17 sample 74220.

	Measured				*PEC Corrected**			
	H_2O ppm	**F ppm**	**S ppm**	**Cl ppm**	**H_2O ppm**	**F ppm**	**S ppm**	**Cl ppm**
Melt Inclusions								
74220 A1	1270	76.2	935		1202	72.1	884	0.00
74220 A2	1410	78.2	849	2.93	1144	63.4	689	2.38
74220 N3	615	71.7	830	1.89	486	56.7	655	1.49
74220 N3repeat	632	70.0	791	1.88	499	55.3	625	1.48
74220 N6	826	60.0	716	2.55	680	49.4	589	2.10
74220 N6repeat	915	61.5	678	2.61	753	50.7	558	2.15
74220 N6repeat	996	61.5	643	2.63	820	50.6	530	2.17
74220 N6repeat	974	67.1	758	2.84	802	55.3	624	2.34
74220 N6repeat	944	63.5	683	2.46	777	52.3	562	2.03
74220 N8	1180	74.5	869	3.02	752	47.5	554	1.92
74220 N8repeat	1092	72.1	855	2.84	696	46.0	545	1.81
74220 N8repeat	1049	71.6	877	2.87	668	45.7	559	1.83
74220 N9 #1	510	50.2	612	1.56	372	36.6	447	1.14
74220 N9 #2	370	59.1	711	1.72	270	43.1	519	1.26
Avg $2\sigma_M$%	*3*	*3*	*3*	*9*				
Matrix Glasses								
74220 A4	12	8.6	293	0.02	10	7.2	245	0.02
74220 A4	13	5.7	248	0.03	11	4.7	207	0.03
74220 N3	9	6.8	353	0.04	8	5.5	286	0.03
74220 N3	12	6.5	333	0.04	10	5.4	276	0.03
74220 N3	10	9.5	457	0.29	8	7.9	378	0.24
74220 N5	7	7.8	297	0.05	6	6.4	242	0.04
74220 N6	6	5.9	295	0.01	5	4.9	244	0.01
74220 N6	30	17.6	382	0.42	25	14.5	316	0.35
74220 N6	25	10.4	318	0.09	21	8.6	263	0.07
74220 N7	5	9.6	490	0.10	4	7.8	397	0.08
74220 N8	14	8.2	317	0.03	11	6.2	240	0.02
74220 N8	13	10.7	425	0.06	10	8.1	321	0.05
74220 N9	8	6.9	396	0.03	6	5.6	322	0.03
74220 N9	15	7.6	333	0.03	13	6.2	272	0.03
Avg $2\sigma_M$%	*10*	*4*	*2*	*41*				

	H_2O ppm	**F ppm**	**S ppm**	**Cl ppm**
D range	0.005 – 0.01	0.03 – 0.06	0.1 – 0.2	0.00005 - 0.00015
Lunar Mantle (5% melting)	79	7.6	193	0.14
Lunar Mantle (30% melting)	409	26	352	0.83

*Correction for post-entrapment crystallization using percentage PEC from Table S1.
D range is the range of mantle-melt partition coefficients used to model lunar mantle concentrations.
"Lunar Mantle" is the lunar mantle source concentration, assuming a range from 5% to 30% batch melting, the range of partition coefficients, and the most enriched corrected melt inclusion composition.

References and Notes

1. R. M. Canup, Dynamics of lunar formation, *Ann. Revs. Astron. Astrophys*. **42**, 441 (2004).

2. S. R. Taylor, in *Origin of the Moon*, W. K. Hartmann, R. J. Phillips, G. J. Taylor, Eds. (Lunar Planet. Inst., Houston, 1986), pp. 125–143.

3. F. Albarede, Volatile accretion history of the terrestrial planets and dynamic implications, *Nature* **461**, 1227 (2009).

4. A. E. Saal *et al.*, Volatile content of the lunar volcanic glasses and the presence of water in the Moon's interior, *Nature* **454**, 192 (2008).

5. F. M. McCubbin *et al*., Nominally anhydrous magmatism on the Moon, *Proc. Natl. Acad. Sci. U.S.A.* **107**, 11223 (2010).

6. J. W. Boyce *et al.*, Lunar apatite with terrestrial volatile abundances, *Nature* **466**, 466 (2010).

7. J. P. Greenwood *et al.*, Hydrogen isotope ratios in lunar rocks indicate delivery of cometary water to the Moon, *Nat. Geosci.* **4**, 79 (2011).

8. J. W. Delano, Pristine lunar glasses: Criteria, data and implications, *J. Geophys. Res.* **91**, D201, 1986.

9. K. A. Kelley *et al.*, Mantle melting as a function of water content beneath back-arc basins, *J. Geophys. Res.* **111**, B09208 (2006).

10. A. M. Shaw, E. H. Hauri, T. P. Fischer, D. R. Hilton, K. A. Kelley, Hydrogen isotopes in Mariana arc melt inclusions: Implications for subduction dehydration and the deep-Earth water cycle, *Earth Planet. Sci. Lett.* **275**, 138 (2008).

11. E. H. Hauri, SIMS analysis of volatiles in silicate glasses, 2: Abundances and isotopes in Hawaiian melt inclusions, *Chem. Geol.* **183**, 115 (2002).

12. J. C. Lassiter, E. H. Hauri, I. K. Nikogosian, H. G. Barsczus, Chlorine-potassium variations in melt inclusions from Raivavae and Rapa, Austral Islands: Constraints on chlorine recycling in the mantle and evidence for brine-induced melting, *Earth Planet. Sci. Lett.* **202**, 525 (2002).

13. N. Shimizu, The geochemistry of olivine-hosted melt inclusions in a FAMOUS basalt ALV519-4-1, *Phys. Earth Planet. Inter.* **107**, 183 (1998).

14. A. M. Shaw, M. D. Behn, S. E. Humphris, R. A. Sohn, Deep pooling of low degree melts and volatile fluxes at the 85°E segment of the Gakkel Ridge: evidence from olivine-hosted melt inclusions and glasses, *Earth Planet. Sci. Lett.* **298**, 311 (2010).

15. H. Y. McSween, R. P. Harvey, Outgased water on Mars: Constraints from melt inclusions in SNC meteorites, *Science* **259**, 1890 (1993).

16. L. Leshin-Watson, I. D. Hutcheon, S. Epstein, E. M. Stolper, Water on Mars: Clues from deuterium/hydrogen and water contents of hydrous phases in SNC meteorites, *Science* **265**, 86 (1994).

17. Detailed information on melt inclusion identification and analytical methods used in this study, as well as all data, are contained in supporting online materials available at *Science* Online.

18. E. Roedder, P. W. Weiblen, Lunar petrology of silicate melt inclusions, Apollo 11 rocks, *Proc. Lunar Sci. Conf.* **1**, 801 (1970).

19. E. Roedder, P. W. Weiblen, Petrology of silicate melt inclusions, Apollo 11 and Apollo 12 and terrestrial equivalents, *Proc. Lunar Sci. Conf.* **2**, 507 (1971).

20. E. Roedder, P. W. Weiblen, Silicate melt inclusions and glasses in lunar soil fragments from the Luna 16 core sample, *Earth Planet. Sci. Lett.* **13**, 272 (1972).

21. N. Klein, M. J. Rutherford, Volcanic gas formed during eruption of Apollo 17 orange glass magma: Evidence from glassy melt inclusions and experiments, *Lunar Planet. Sci.* **29**, 1448 (1998).

22. C. M. Weitz, M. J. Rutherford, J. W. Head III, D. S. McKay, Ascent and eruption of lunar high-titanium magma as inferred from the petrology of the 74001/2 drill core, *Met. Planet. Sci.* **34**, 527 (1999).

23. D. J. Bombardieri, M. D. Norman, V. S. Kamenetsky, L. V. Danyushevsky, Major element and primary sulfur concentrations in Apollo 12 mare basalts: The view from melt inclusions, *Met. Planet. Sci.* **40**, 679 (2005).

24. A. E. Saal, E. H. Hauri, C. H. Langmuir, M. R. Perfit, Vapour undersaturation in primitive mid-ocean-ridge basalt and the volatile content of the Earth's upper mantle, *Nature* **419**, 451 (2002).

25. A. Jambon, J. L. Zimmerman, Water in oceanic basalts: Evidence for dehydration of recycled crust, *Earth Planet. Sci. Lett.* **101**, 323 (1990).

26. P. Michael, Regionally distinctive sources of depleted MORB: Evidence from trace elements and H2O, *Earth Planet. Sci. Lett.* **131**, 301 (1995).

27. J. Dixon, L. Leist, C. Langmuir, J. G. Schilling, Recycled dehydrated lithosphere observed in plume-influenced mid-ocean-ridge basalt, *Nature* **420**, 385 (2002).

28. Z. D. Sharp, C. K. Shearer, K. D. McKeegan, J. D. Barnes, Y. Q. Wang, The chlorine isotope composition of the Moon and implications for an anhydrous mantle, *Science* **329**, 1050 (2010).

29. K. Pahlevan, D. J. Stevenson, Equilibration in the aftermath of the lunar-forming giant impact, *Earth Planet. Sci. Lett.* **262**, 438 (2007).

30. W. C. Feldman, S. Maurice, D. J.. Lawrence, R. C. Little, S. L. Lawson, O. Gasnault, R. C. Wiens, B. L. Barraclough, R. C. Elphic, T. H. Prettyman, J. T. Steinberg, A. B. Binder, Evidence for water ice near the lunar poles, *J. Geophys. Res.* **106**, 23231 (2001).

31. A. P. S. Crotts, Lunar outgassing, transient phenomena, and the return to the Moon, I: Existing data, *Astrophys. J.* **687**, 692 (2008).

32. K. Koga, E. H. Hauri, M. M. Hirschmann, D. R. Bell, Hydrogen concentration analyses using SIMS and FTIR: Comparison and calibration for nominally anhydrous minerals, *Geochem. Geophys. Geosys*. **4**, doi: 2002GC000378 (2002).

33. E. H. Hauri, G. A. Gaetani, T. H. Green, Partitioning of water during melting of the Earth's upper mantle at H_2O-undersaturated conditions, *Earth Planet. Sci. Lett.* **248**, 715 (2006).

34. E. H. Hauri, J. Wang, J. E. Dixon, P. L. King, C. Mandeville, S. Newman, SIMS Investigations of volatiles in silicate glasses, 1: Calibration, matrix effects and comparisons with FTIR, *Chem. Geol.* **183**, 99 (2002).

35. J. Longhi, D. Walker, J. F. Hays, The distribution of Fe and Mg between olivine and lunar basaltic liquids, *Geochim. Cosmochim. Acta* **42**, 1545 (1978).

36. T. Wagner, T. L. Grove, Experimental constraints on the origin of lunar high-Ti ultramafic glasses, *Geochim. Cosmochim. Acta* **61**, 1315 (1997).

37. D. Xirouchakis, M. M. Hirschmann, J. A. Simpson, The effect of titanium on the silica content and on mineral-liquid partitioning of mantle-equilibrated melts, *Geochim. Cosmochim. Acta* **65**, 2201 (2001).